*fibers*

MDPI

*Article*

# Kapok-Derived Super Hollow Porous Carbon Fibers and Their Greenhouse Gases Adsorption

**Hun-Seung Jeong [1,2,†], Cheol-Ki Cho [1,2,†], Dong-Chul Chung [3,*], Kay-Hyeok An [1,4,*] and Byung-Joo Kim [1,4,*]**

[1] Materials Application Research Institute, Jeonju University, Jeonju 55069, Republic of Korea; hunseung.jeong@jj.ac.kr (H.-S.J.); joc0406@naver.com (C.-K.C.)
[2] Department of Energy Science, Sungkyunkwan University, Suwon 16419, Republic of Korea
[3] Department of Organic Materials and Textile Engineering, Jeonbuk National University, Jeonju 54896, Republic of Korea
[4] Department of Materials Science and Chemical Engineering, Jeonju University, Jeonju 55069, Republic of Korea
* Correspondence: sonagiii0523@gmail.com (D.-C.C.); khandragon@jj.ac.kr (K.-H.A.); kimbj2015@gmail.com (B.-J.K.)
† These authors contributed equally to this work.

## Abstract

Industrialization and modernization have significantly improved the quality of life but have also led to substantial pollution. Cost-effective technologies are urgently needed to mitigate emissions from major polluting sectors, such as the automotive and transport industries. In this study, we synthesized naturally derived, kapok-based porous carbon fibers (KP-PCFs) with hollow structures. We investigated their adsorption/desorption behavior for the greenhouse gas n-butane following ASTM D5228 standards. Scanning electron microscopy and X-ray diffraction analyses were conducted to examine changes in fiber diameter and crystalline structure under different activation times. The micropore properties of KP-PCFs were characterized using Brunauer–Emmett–Teller, *t*-plot, and non-localized density functional theory models based on $N_2$/77K adsorption isotherm data. The specific surface area and total pore volume ranged from 500 to 1100 $m^2/g$ and 0.24 to 0.60 $cm^3/g$, respectively, while the micropore and mesopore volumes were 0.20–0.45 $cm^3/g$ and 0.04–0.15 $cm^3/g$, respectively. With increasing activation time, the n-butane adsorption capacity improved from 62.2% to 73.5%, whereas retentivity (residual adsorbate) decreased from 6.0% to 1.3%. The adsorption/desorption rate was highly correlated with pore diameter: adsorption capacity was highest for diameters of 1.5–2.5 nm, while retentivity was greatest for diameters of 3.5–5.0 nm.

**Keywords:** kapok; hollow fiber; porous carbon; n-Butane adsorption/desorption

check for updates

Academic Editor: David P. Harper

Received: 18 March 2025
Revised: 19 June 2025
Accepted: 30 June 2025
Published: 4 July 2025

**Citation:** Jeong, H.-S.; Cho, C.-K.; Chung, D.-C.; An, K.-H.; Kim, B.-J. Kapok-Derived Super Hollow Porous Carbon Fibers and Their Greenhouse Gases Adsorption. *Fibers* **2025**, *13*, 92. https://doi.org/10.3390/fib13070092

**Copyright:** © 2025 by the authors. Licensee MDPI, Basel, Switzerland. This article is an open access article distributed under the terms and conditions of the Creative Commons Attribution (CC BY) license (https://creativecommons.org/licenses/by/4.0/).

## 1. Introduction

Since the First Industrial Revolution, advancements in science, technology, and industry have significantly improved the quality of life. However, this progress has also led to excessive fossil fuel consumption and the emission of carbon dioxide ($CO_2$), sulfur oxides (SOx), nitrogen oxides (NOx), volatile organic compounds (VOCs), and other air pollutants, contributing to severe global warming [1–5]. Greenhouse gases have caused various environmental issues, including ecosystem degradation and rising sea levels, while VOCs can have direct and potentially fatal effects on the human respiratory and circulatory systems [6–8].

To mitigate these issues, environmental regulations for internal combustion engine vehicles have been strengthened, increasing the demand for high-performance adsorbents in exhaust emission control systems. Evaporative emissions primarily originate from fuel tanks during parking or engine start-up, where they are adsorbed by canister adsorbents and later desorbed and combusted in the engine while driving [9–11]. Canister adsorbents must withstand repeated adsorption–desorption cycles, necessitating a pore structure with excellent adsorption and desorption characteristics [12–15]. Various adsorbents have been studied for controlling hydrocarbon vapors such as n-butane. For example, mesoporous zeolite molecular sieves have been reported to exhibit high adsorption capacities (118.2 mg/g) for n-butane under ambient conditions due to their well-defined pore channels [16]. MOF-derived carbon composites and polymer-coated porous structures have also demonstrated promising butane working capacity [17]. Additionally, biochar-silica hybrids and activated polymer resins are under investigation as cost-effective and regenerable alternatives [18]. These studies highlight the need for adsorbents that balance high capacity, desorption efficiency, and stability—criteria that porous carbon fibers (PCFs) aim to satisfy. Porous carbon fibers (PCFs) are suitable as canister adsorbents due to their rapid adsorption rates for low-concentration substances, attributed to the exposed micropores on their surfaces, and their efficient desorption, facilitated by wedge-shaped pore structures. These properties enable PCFs to outperform pellet-formed and powdered absorbents [19–23]. However, the production of PCFs involves complex processing and fiber-shaped precursors, resulting in relatively high production costs [24–28]. Further research is necessary to identify cost-effective alternatives to conventional precursors.

Kapok fiber (KF), derived from the fruit of the kapok tree, exhibits excellent resilience, a soft texture, and low production costs, making it a popular material in textile applications [29]. KF has a hollow internal structure, providing a unique morphology that facilitates efficient carbonization and activation processes. During pyrolysis in an inert atmosphere, the volatile components in KF are released, while the remaining carbon framework retains its fibrous and porous structure. This inherent property makes KF a promising and cost-effective precursor for producing porous carbon materials. Additionally, its abundance and low production costs enhance its feasibility for large-scale applications in environmental and industrial sectors.

For instance, Wang et al. prepared activated carbon fibers from kapok using chemical activation with diammonium hydrogen phosphate, achieving a specific surface area of 548 $m^2/g$, and applied the material to adsorb phenol and methylene blue from aqueous solution [30]. Thazin et al. synthesized kapok-based activated carbon fibers via KOH chemical activation, reaching 1267 $m^2/g$, and investigated their use in supercapacitor electrodes [31]. Yu et al. fabricated hierarchical porous carbons from kapok fibers through KOH activation and surfactant-assisted modification, yielding a high surface area of 2375 $m^2/g$, and applied them for removal of organic dyes in liquid phase systems [32].

In this study, we evaluated the potential of natural KF as a precursor for synthesizing hollow PCFs through steam-based physical activation. We analyzed the microstructural and pore structure changes in kapok-based PCFs (KP-PCFs) produced at various activation times and examined variations in diameter and thickness resulting from carbonization and activation. Finally, we elucidated the relationship between pore structure and the butane adsorption/desorption behavior of KP-PCFs developed at different activation times, which determines carbon canister performance.

## 2. Materials and Methods

### *2.1. Carbonization of Kapok Fiber*

Prior to carbonization, KFs were dried in an 80 °C oven for 24 h to completely remove residual moisture. Subsequently, KF (20 g) was placed in an alumina boat crucible (length: 17 cm) inside a horizontal quartz tube furnace. Carbonization was performed by heating the sample to 900 °C at a rate of 10 °C/min and maintaining this temperature for 1 h. During heating, high-purity nitrogen ($N_2$, 99.999%) was continuously introduced into the quartz tube at 200 mL/min to prevent oxidation of the KFs by oxygen ($O_2$) or carbon dioxide ($CO_2$) from the ambient air. Additionally, this setup minimized the retention of volatile substances generated during carbonization, reducing interference with pore structure formation. The nitrogen flow was maintained until the furnace naturally cooled to room temperature to prevent further oxidation or combustion.

The carbonization process resulted in a carbon yield of 19.0% for kapok fibers. While this yield falls within the range observed for biomass precursors such as sugarcane bagasse and wood, it is relatively low compared to the theoretical maximum carbon yield of cellulose. The carbonization behavior of kapok fibers was further analyzed through TGA data (Figure S1), providing insights into the decomposition process and the resulting carbon yield.

### *2.2. Physical Steam Activation*

Carbonized KF (KF-C, 3.5 g) was placed in a 17 cm alumina boat crucible at the center of an activation tube furnace (Inconel, 1200 mm × 80 mm). Activation was performed by heating the sample to 900 °C at a rate of 10 °C/min while continuously introducing high-purity $N_2$ 99.999%) at 200 mL/min. Upon reaching 900 °C, $N_2$ gas was replaced with steam to initiate physical activation, maintaining a steam flow rate of 0.5 mL/min. The activation times were set to 5, 10, 15, and 20 min. After activation, nitrogen gas was reintroduced during natural cooling to room temperature to prevent additional oxidation reactions. The resulting PCFs were designated as KP-PCF-5, KP-PCF-10, KP-PCF-15, and KP-PCF-20 according to their respective activation times.

### *2.3. Surface Morphology of Porous Carbon Fibers*

The morphological differences between KP-PCFs produced at different activation times were analyzed using field emission scanning electron microscopy (FE-SEM, SU8600, Hitachi, Tokyo, Japan) at an acceleration voltage of 10 kV. All samples were examined at a magnification of 3000×. Additionally, variations in fiber diameter and thickness were evaluated across the samples.

### *2.4. Functional Group Analysis of Porous Carbon Fibers*

Changes in the functional groups of KP-PCFs at different activation times were analyzed using temperature-programmed reduction (TPR) with a BELCAT II system (Microtrac BEL, Japan). The gases evolved during the TPR process were examined using FT-IR). The TPR analysis was performed under an argon atmosphere (50 cc/min) with a heating rate of 15 °C/min, from 25 °C to 900 °C. During this process, CO and $CO_2$ gases were detected via FT-IR, and their evolution profiles at various temperatures were used to assess oxygen-containing functional groups (OFGs).

### *2.5. Microcrystalline Structure of Porous Carbon Fibers*

We analyzed the microcrystalline structural characteristics of KP-PCFs using X-ray diffraction (XRD) spectroscopy (Miniflex, Rigaku, Tokyo, Japan) over a 10–60° range at a scan rate of 2°/min, employing Cu-K$\alpha$ radiation (1.5406 Å). To examine differences in the

crystalline structure at different activation times, all diffraction patterns were fitted using Gaussian calculations, from which the central diffraction angle and the full width at half maximum of each crystallite peak were determined. The interplanar distances (d002, d10l) of KP-PCFs were calculated using Bragg's Equation (1). Additionally, crystallite size (La) and height (Lc) were determined based on Scherrer's Equation (2) [33].

$$d(\text{Å}) = \frac{\lambda}{2sin\theta} \quad (1)$$

$$L(\text{Å}) = \frac{K\lambda}{Bcos\theta} \quad (2)$$

Here, $\lambda$ represents the wavelength of the incident X-ray (1.5406 Å), and B is the full width at half maximum (FWHM) of the diffraction peak. The shape factor k was set to 0.9 for the (002) peak (used to calculate Lc) and 1.84 for the (10l) peak (used to calculate La), based on standard values commonly adopted for carbon materials [33].

### *2.6. Pore Characteristics of Porous Carbon Fibers*

The pore characteristics of KP-PCFs were analyzed using an $N_2$/77K isothermal adsorption analyzer (BELSORP-maxII, MicrotracBEL, Osaka, Japan). Before analysis, all KP-PCF samples were degassed at 300 °C for 12 h under a pressure of <0.1 Pa. The specific surface area was calculated using the Brunauer–Emmett–Teller (BET) equation, while the total pore volume was determined from the amount of nitrogen adsorbed at $P/P_0$ = 0.99 [34]. The micropore volume was calculated using the *t*-plot method, based on adsorbed gas thickness in the range of 0.6–1.6 nm [35]. The mesopore volume was obtained by subtracting the micropore volume from the total pore volume. The pore size distribution (PSD) of KP-PCFs was determined using a nonlocalized density functional theory (NLDFT) model, fitted with a slit model method, and computed using the log-normal method [36].

### *2.7. Measurement of Butane Working Capacity*

The butane working capacity (BWC) measurements were conducted by ASTM D5228 [37]. Each KP-PCF sample (~1.0 g) was packed into a U-shaped cell of the same volume for analysis. Before analysis, all samples were degassed by flowing high-purity $N_2$ (99.999%) at 300 mL/min. Butane adsorption was performed at a flow rate of 250 mL/min. If saturation was not reached in the first measurement, the adsorption experiment was repeated at 10 min intervals using the same flow rate until a stable KP-PCF weight was achieved. The samples were then degassed for 40 min at a flow rate of 300 mL/min. This process was repeated three times, and the average of the three measurements was used. Butane activity (BA), butane retention (BR), and BWC were calculated using Equations (3)–(5) below.

$$\text{BA} = \frac{\text{weight of butane adsorbed PCF} - \text{original weight of PCF}}{\text{original weight of PCF}} \times 100 \quad (3)$$

$$\text{BR} = \frac{\text{weight of PC}F\text{ after nitrogen purging} - \text{original weight of PCF}}{\text{original weight of PCF}} \times 100 \quad (4)$$

$$\text{BWC} = \frac{\text{weight of butane adsorbed PCF} - \text{weight of PCF after nitrogen purging}}{\text{original weight of PCF}} \times 100 \quad (5)$$

## 3. Results and Discussion

### *3.1. SEM Analysis*

FE-SEM analysis revealed that the KFs had a hollow structure, with an initial diameter and wall thickness of 18.1 μm and 1.4 μm, respectively (Figure 1a and Figure S2). As activation time increased from 5 to 20 min, the diameter and wall thickness further decreased from 14.6 μm to 11.2 μm and from 0.65 μm to 0.41 μm, respectively, due to progressive oxidation of the carbon surface. In KF-C, the diameter decreased to 15.1 μm, while the wall thickness was reduced to 0.65 μm, likely due to volume contraction associated with thermal decomposition and structural changes during carbonization. As the activation time increased, both the fiber diameter and wall thickness gradually decreased. KP-PCFs activated for 5 min exhibited a diameter of 14.6 μm and a wall thickness of 0.65 μm, whereas those activated for 20 min had a diameter of 11.2 μm and a wall thickness of 0.41 μm. These reductions were attributed to the oxidation of surface carbon through reactions with steam during activation. The progressive decrease in both diameter and wall thickness with longer activation times suggests that oxidation is the primary factor driving these changes.

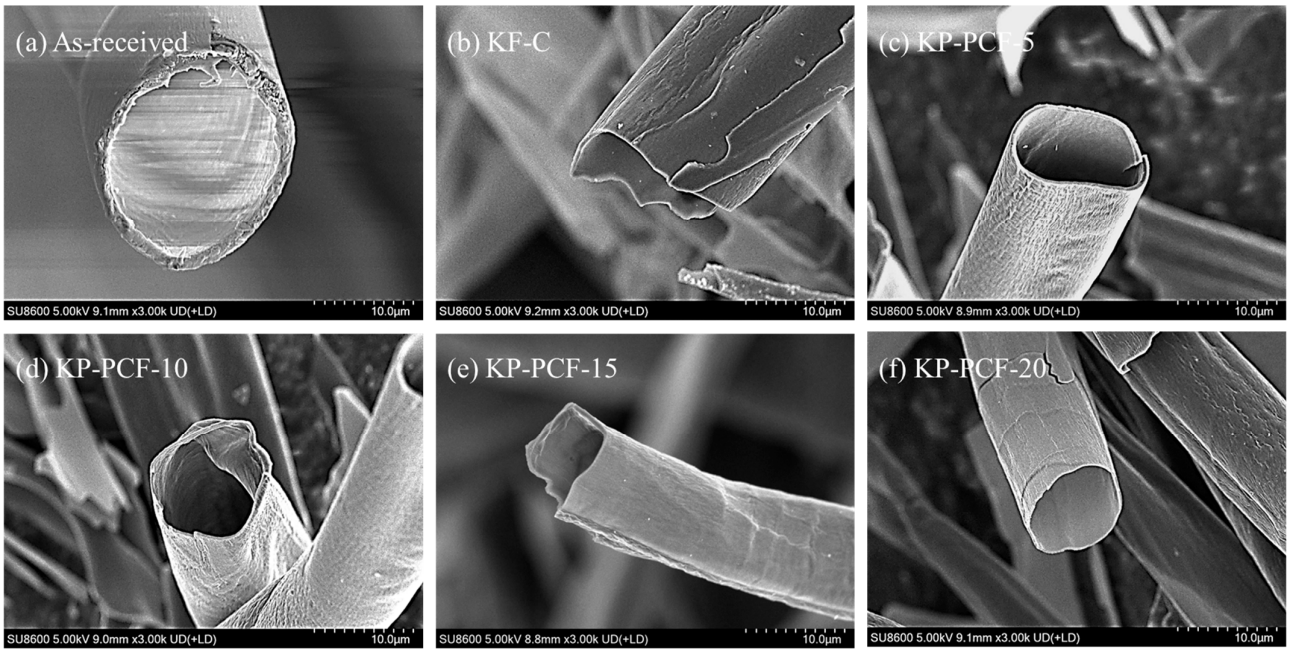



**Figure 1.** Field emission scanning electron microscope images of kapok-based porous carbon fiber. (**a**) As-received, (**b**) KF-C, (**c**) KP-PCF-5, (**d**) KP-PCF-10, (**e**) KP-PCF-15, and (**f**) KP-PCF-20.

### *3.2. Temperature-Programmed Desorption Infrared Spectroscopy Analysis*

TPR-IR was employed to analyze the oxygen-containing functional groups (OFGs) of porous carbon fibers (PCFs) by observing changes in gas concentration as the temperature increased linearly. KP-PCFs were activated under varying activation times. The changes in OFGs of KP-PCFs under different activation conditions were investigated using TPR-IR. During the TPR process, KP-PCFs underwent thermal decomposition, and the evolved gases were detected using FT-IR. The decomposition temperatures and the types of gases released varied depending on the specific OFGs present.

Figure 2 presents the TPR-IR curves of KP-C and KP-PCFs. CO and $CO_2$ emissions from KP-C and KP-PCFs were detected within the temperature ranges of 200–1000 °C and 100–900 °C, respectively. The functional groups corresponding to $CO_2$ were primarily carboxyl and lactone groups, with a slight increase in carboxyl groups observed as activation time increased. Similarly, the functional groups associated with CO were mainly hydroxyl and carboxyl groups. In KP-C, carboxyl groups were dominant, with hydroxyl

groups present in minor amounts. As activation time increased, hydroxyl groups exhibited a decreasing trend, while carboxyl groups increased.

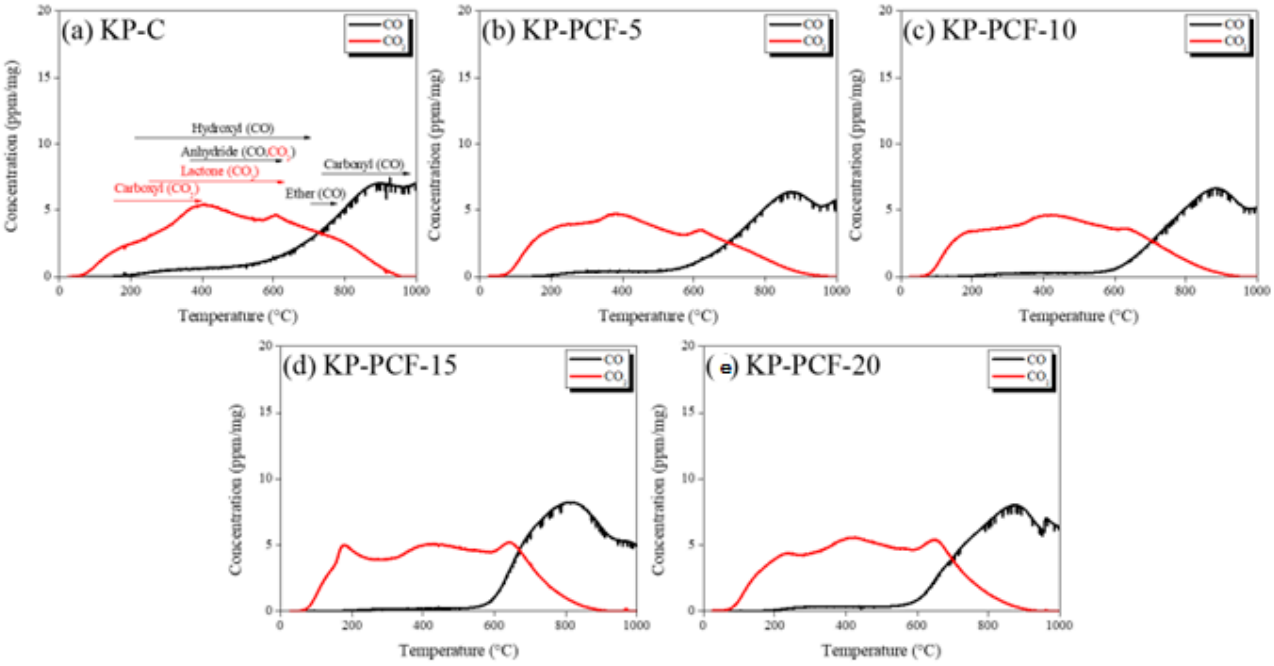



**Figure 2.** TPR-IR curves of KP-C and KP-PCFs under varying activation times. (**a**) KF-C, (**b**) KP-PCF-5, (**c**) KP-PCF-10, (**d**) KP-PCF-15, and (**e**) KP-PCF-20.

Overall, as activation time increased, carboxyl and carbonyl groups tended to increase, while hydroxyl groups decreased, likely due to exposure to high temperatures (900 °C). This trend highlights the impact of activation time and temperature on the evolution of oxygen-containing functional groups in KP-PCFs.

### *3.3. X-Ray Diffraction Analysis*

XRD is a valuable analytical method for examining the crystalline structure of carbon materials [38,39]. To establish a baseline for comparison, we first analyzed the XRD pattern of KF before carbonization. The XRD results revealed the semi-crystalline nature of KF, characterized by a prominent diffraction peak at approximately 21.9°, corresponding to the (200) crystalline plane of cellulose I. Additional low-intensity peaks were observed around 15°, which are attributed to the (110) and (1–10) planes, in agreement with typical diffraction patterns of cellulose I. These findings indicate the coexistence of crystalline and amorphous regions within the kapok fibers. The semi-crystalline structure suggests that the crystalline regions provide structural integrity, while the amorphous regions facilitate pore formation during carbonization through the release of volatile components.

Following carbonization and activation, we used XRD to investigate changes in the crystalline structure relative to activation time (Figure 3). Generally, as the crystalline structure of carbon materials develops, the C(002) peak becomes sharper, and the diffraction angle approaches 26.5° [40,41]. However, the broad XRD curve indicated that, with increasing activation time, peak intensities decreased due to increased burn-off.

The microstructural parameters are presented in Figure 3b. The crystallite height (Lc), calculated from the (002) plane peak, increased continuously as the activation time was extended to 15 min; however, a decrease was observed at 20 min, likely due to the preferential oxidation and removal of amorphous carbon and small crystallites during early activation, leading to an increase in average crystallite size. Further activation initiated the oxidation of crystallites. The crystallite width (La), derived from the (10l) plane peak,

exhibited a similar trend to that of Lc: it initially increased up to 15 min, which can be attributed to the oxidation and removal of amorphous carbon and small crystallites. However, prolonged activation beyond 15 min initiated the oxidation of crystallite edges, resulting in a decrease in La due to structural degradation [14,41].

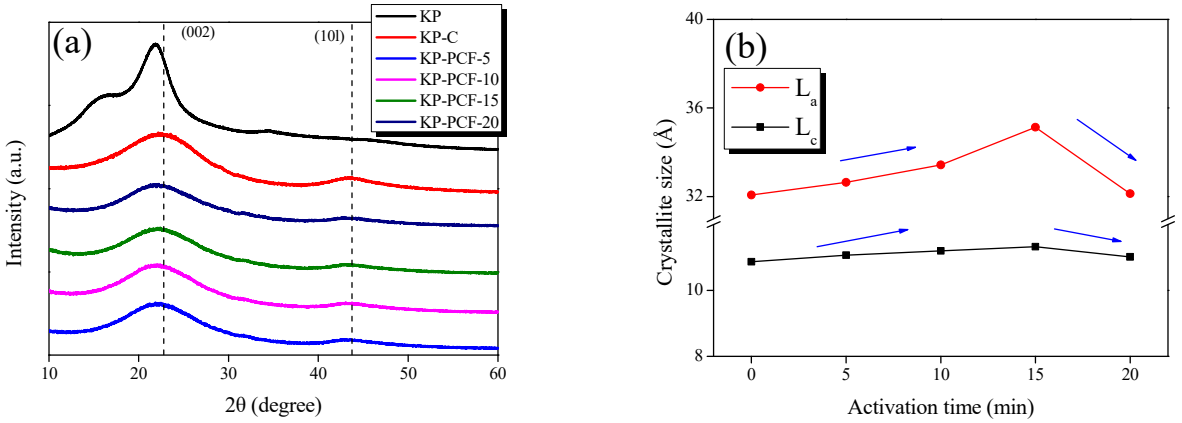



**Figure 3.** (**a**) X-ray diffraction patterns and (**b**) crystallite sizes of KP-PCFs according to the various activation times.

### *3.4. $N_2$/77K Isotherm Adsorption/Desorption Analysis*

$N_2$/77K isothermal adsorption/desorption analysis is a highly effective method for characterizing the pore properties of porous materials [42–44]. In Figure 4, filled symbols indicate $N_2$ adsorption, while unfilled symbols indicate desorption. We utilized $N_2$/77K isothermal adsorption/desorption analysis to examine the pore characteristics of KP-PCFs produced with different activation times (Figure 4). The adsorption/desorption curves of KP-PCFs initially showed an increase in $N_2$ adsorption with longer activation times, followed by a decline. The $N_2$/77K isothermal adsorption/desorption curve was classified as Type I according to the International Union of Pure and Applied Chemistry, with H4 hysteresis loops [45]. Type I curves are typical of porous materials in which monolayer adsorption occurs between the pore walls and adsorbate, a phenomenon commonly observed in materials with well-developed microporosity [45]. Thus, the manufactured KP-PCFs exhibited well-developed micropores. Additionally, as activation time increased, $P/P_0 < 0.1$ rose to 15 min of activation but declined by 20 min, likely due to the conversion of some micropores to mesopores as a result of crystallite edge oxidation.

Table 1 presents the textural properties of KP-PCFs produced with different activation times. For comparison, the KP-C sample obtained through carbonization without activation exhibited a specific surface area of approximately 500 $m^2/g$. The formation of pores in KP-C is attributed to the decomposition of cellulose, hemicellulose, and lignin during the carbonization process. These components undergo thermal decomposition under an inert atmosphere, releasing volatile gases such as CO, $CO_2$, and $H_2O$, which create pores within the carbon matrix. Although the pore structure in KP-C is less developed than in activated samples, this initial porosity serves as a foundation for subsequent activation processes, which further enhance surface area and pore volume. During steam-based physical activation, pore development was primarily driven by oxidation of the carbon framework, particularly at the edges of crystalline regions. As shown in Table 1, this structural transformation is accompanied by a progressive decrease in activation yield, from 60.0% at 5 min to 29.0% at 20 min, confirming that increased activation time leads to higher burn-off. The specific surface area and total pore volume ranged from 500 to 1100 $m^2/g$ and 0.24 to 0.60 $cm^3/g$, respectively. In particular, the KP-PCF-15 sample exhibited the highest specific surface area (1100 $m^2/g$) with a corresponding

activation yield of 53.0%, indicating an optimal balance between porosity enhancement and structural retention. While micropore and mesopore volumes increased with activation time, both began to decline slightly at 20 min, likely due to overburning of the carbon matrix. Thazin et al. (2022) reported a specific surface area of 487 $m^2/g$ for KP-PCFs produced via KOH activation [31], while Chung et al. (2013) observed a maximum specific surface area of 753 $m^2/g$ using steam activation [46]. These variations highlight the differences in pore characteristics and material retention depending on activation method and fabrication conditions.

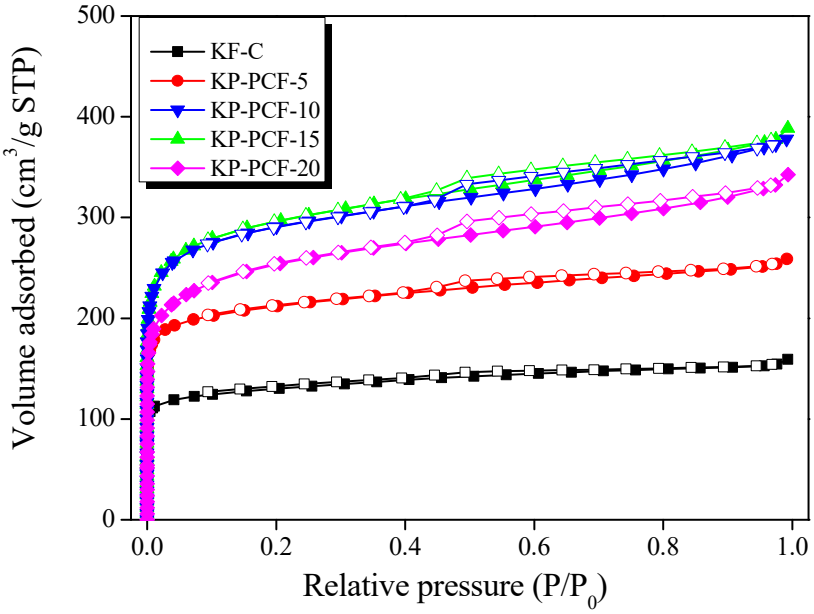



**Figure 4.** $N_2$/77K isothermal adsorption/desorption curves of KP-PCFs as a function of various activation times.

**Table 1.** Textural parameters of KP-PCFs produced with different activation times.

| Sample | $S_{BET}$ [a] ($m^2/g$) | $V_{total}$ [b] ($cm^3/g$) | $V_{micro}$ [c] ($cm^3/g$) | $V_{meso}$ [d] ($cm^3/g$) | $F_{micro}$ [e] (%) | Activation Yield (%) | Reference |
|---|---|---|---|---|---|---|---|
| KF-C | 500 | 0.24 | 0.20 | 0.04 | 83.3 | - | This study |
| KP-PCF-5 | 810 | 0.40 | 0.33 | 0.07 | 82.5 | 60.0 | |
| KP-PCF-10 | 1080 | 0.58 | 0.44 | 0.14 | 75.9 | 53.0 | |
| KP-PCF-15 | 1100 | 0.60 | 0.45 | 0.15 | 75.0 | 41.0 | |
| KP-PCF-20 | 920 | 0.53 | 0.38 | 0.15 | 71.7 | 29.0 | |
| ACF-300 | 487 | 0.26 | 0.21 | 0.05 | 80.8 | - | [31] |
| KAHCF | 753 | 0.62 | - | - | - | - | [46] |

[a] $S_{BET}$: Specific surface area, BET method; $\frac{P}{v(P_0-P)} = \frac{1}{v_m} + \frac{c-1}{v_m c} \cdot \frac{P}{P_0}$. [b] $V_{total}$: Total pore volume, amount adsorbed at $P/P_0 = 0.99$. [c] $V_{micro}$: Micropore volume, *t*-plot. [d] $V_{meso}$: Mesopore volume, $V_{total} - V_{micro}$. [e] $F_{micro}$: Micropore volume fraction, $V_{total}/V_{micro} \times 100$.

Figure 5 presents the PSD curves of KP-PCFs obtained using the NLDFT equation. Pore sizes ranged from 1.0 to 3.0 nm as activation time increased. Between 5 and 15 min, pores measuring 0.7–2.0 nm developed, whereas at 20 min, fewer pores in the 0.7–1.0 nm range were observed. Additionally, pore sizes of 1.5–2.0 nm increased linearly with activation time. These results suggest that KP-PCFs developed pores of 0.7–2.0 nm due to amorphous and edge oxidation of crystallites, while excessive oxidation at 20 min reduced the formation of narrower micropores.

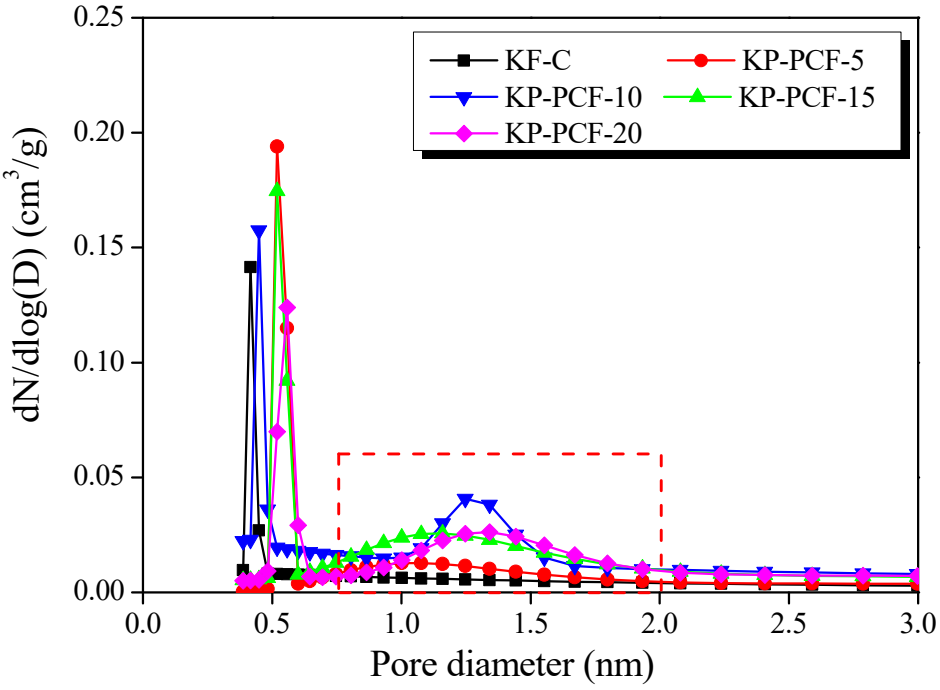



**Figure 5.** Pore size distribution of KP-PCFs produced with various activation times.

### *3.5. Butane Working Capacity*

Figure 6 presents the BWC of KP-PCFs produced with varying activation times, along with the BA and BR values calculated from n-butane adsorption and desorption experiments. As activation time increased, BA rose from 62.2% to 73.5%, whereas BR decreased from 6.0% to 1.3%, likely due to the expansion of micropore and mesopore volumes with prolonged activation. BA and BR were correlated with the volumes of micropores and mesopores, respectively, with BA closely associated with pore diameters of 1.5–2.0 nm and BR with diameters of 3.0–5.0 nm [47]. BA exhibited a notable increase at 10 min of activation, likely due to the development of 1.0–2.0 nm pores. The linear expansion of mesopores with increasing activation time was presumed to account for the corresponding linear decrease in BR.

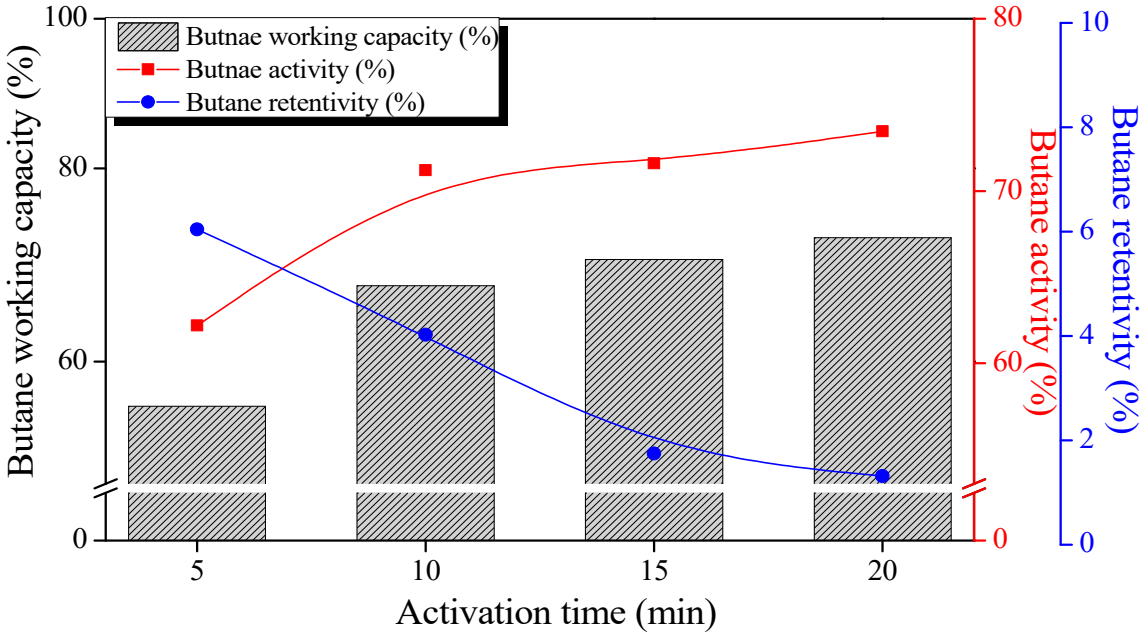



**Figure 6.** n-Butane adsorption/desorption parameters of KP-PCFs produced with different activation times.

Figure 7 illustrates the factors influencing changes in BA and BR, plotted against pore volume as a function of pore diameter. These values were calculated using the NLDFT method and presented in 0.5 nm increments along the *X*-axis. BA and BR exhibited strong correlations with pore volumes of 1.5–2.5 nm and 3.5–5.0 nm, respectively. Notably, BA showed a strong correlation (>0.95) with pores measuring 1.5–2.0 nm, while BR was associated with an increasing average pore diameter. These findings are consistent with previous reports, which indicate that butane adsorption and desorption capacities are strongly influenced by sub-micropores (1.5–2.0 nm) and mesopores (>3 nm), respectively [47].

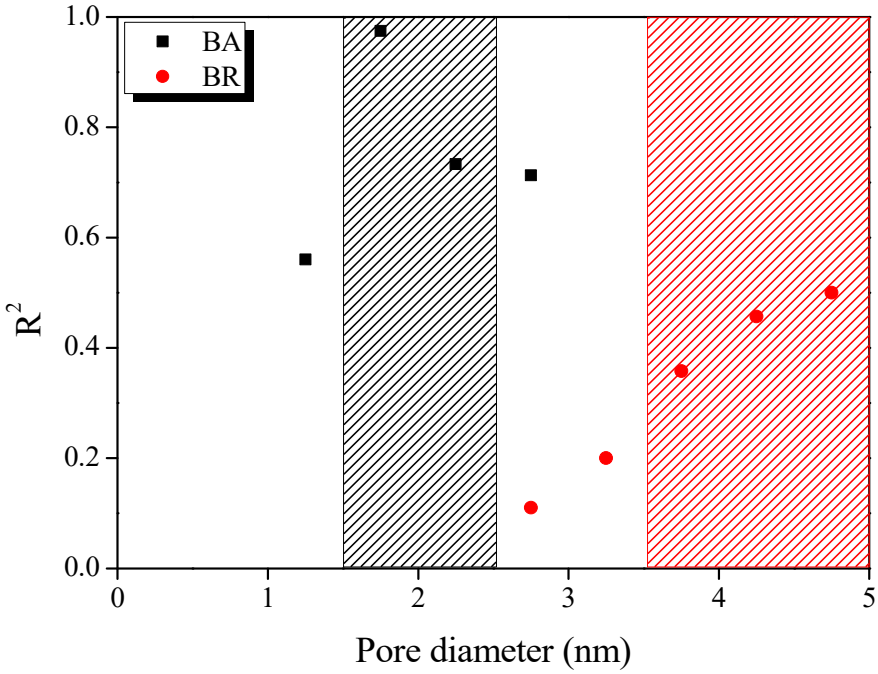



**Figure 7.** Correlations between the butane activity and retentivity of kapok-based porous carbon fibers and pore diameter.

## 4. Conclusions

KP-PCFs were prepared from KFs at various activation times for n-butane adsorption. The specific surface area of the KP-PCFs increased from 500 to 1100 $m^2/g$ with longer activation times. The micropore and mesopore volumes ranged from 0.20 to 0.45 $cm^3/g$ and 0.04 to 0.15 $cm^3/g$, respectively. The micropore volume increased over the first 15 min of activation due to the oxidation of amorphous structures during physical activation, whereas the mesopore volume increased thereafter as a result of crystallite edge oxidation. The adsorption capacity of n-butane increased linearly with activation time, whereas the retention amount decreased linearly. BA was correlated with pore sizes of 1.5–2.0 nm, while BR was associated with pore diameters greater than 3.0 nm. These results demonstrate the potential of KP-PCFs as efficient adsorbents for hydrocarbon vapor recovery applications such as fuel vapor control in automotive carbon canisters. Future work should evaluate their long-term regeneration stability and performance under dynamic operation conditions.

**Supplementary Materials:** The following supporting information can be downloaded at: https://www.mdpi.com/article/10.3390/fib13070092/s1, Figure S1. TGA curve of kapok fiber under a nitrogen atmosphere, Figure S2. SEM images and standard deviation of fiber diameter and wall thickness for KP, KP-C and KP-PCFs under varying activation times. (a) As-received, (b) KF-C, (c) KP-PCF-5, (d) KP-PCF-10, (e) KP-PCF-15, (f) KP-PCF-20 and (g) Fiber diameter and wall thickness changes with activation time, Table S1. Microstructural Parameters of KF-PCFs as a Function of Activation Times.

**Author Contributions:** Conceptualization, B.-J.K. and K.-H.A.; Data curation, H.-S.J. and B.-J.K.; Formal analysis, H.-S.J. and C.-K.C.; Funding acquisition, B.-J.K. and K.-H.A.; Investigation, H.-S.J. and C.-K.C.; Methodology, B.-J.K., D.-C.C. and H.-S.J.; Project administration, B.-J.K.; Resources, B.-J.K. and K.-H.A.; Software, H.-S.J., C.-K.C. and D.-C.C.; Supervision, B.-J.K.; Validation, H.-S.J., C.-K.C. and B.-J.K.; Visualization, H.-S.J.; Writing—original draft, H.-S.J. and C.-K.C.; Writing—review and editing, H.-S.J. and B.-J.K. All authors have read and agreed to the published version of the manuscript.

**Funding:** This work was supported by the Material Parts Technology Development Project (no. RS-2024-00434503); Carbon Industry Foundation Project (no. 20016795) funded by the Ministry of Trade, Industry, and Energy; the Regional Innovation System & Education (RISE) initiative, funded by the Ministry of Education and administered by the National Research Foundation of Korea (NRF); the Korea Evaluation Institute of Industrial Technology project (no. 20017563) for the development of single-walled carbon nanotube-binder integrated conductive material and its application to high energy-density secondary battery technology; and the Ministry of Trade, Industry, and Energy Technology Innovation Program (Project No. 20013038). This research was supported by the Jeonju University Research Year.

**Data Availability Statement:** The original contributions presented in this study are included in the article/Supplementary Material. Further inquiries can be directed to the corresponding authors.

**Conflicts of Interest:** The authors declare no conflicts of interest.

## References

1. Shahbazi, A.; Nasab, B.R. Carbon Capture and Storage (CCS) and its Impacts on Climate Change and Global Warming. *J. Pet. Environ. Biotechnol.* **2016**, *7*, 1000291. [CrossRef]
2. Bhaskaran, A.; Sharma, D.; Roy, S.; Singh, S.A. Technological Solutions for $NO_x$, $SO_x$, and VOC Abatement: Recent Breakthroughs and Future Directions. *Environ. Sci. Pollut. Res.* **2023**, *30*, 91501–91533. [CrossRef]
3. Martins, F.; Felgueiras, C.; Smitkova, M.; Caetano, N. Analysis of Fossil Fuel Energy Consumption and Environmental Impacts in European Countries. *Energies* **2019**, *12*, 964. [CrossRef]
4. Lelieveld, J.; Klingmüller, K.; Pozzer, A.; Burnett, R.T.; Haines, A.; Ramanathan, V. Effects of Fossil Fuel and Total Anthropogenic Emission Removal on Public Health and Climate. *Proc. Natl. Acad. Sci. USA* **2019**, *116*, 7192–7197. [CrossRef]
5. Peter, S.C. Reduction of $CO_2$ to Chemicals and Fuels: A Solution to Global Warming and Energy Crisis. *ACS Energy Lett.* **2018**, *3*, 1557–1561. [CrossRef]
6. Manisalidis, I.; Stavropoulou, E.; Stavropoulos, A.; Bezirtzoglou, E.A. Environmental and Health Impacts of Air Pollution: A Review. *Front. Public Health* **2020**, *8*, 14. [CrossRef]
7. Zhou, X.; Zhou, X.; Wang, C.; Zhou, H. Environmental and Human Health Impacts of Volatile Organic Compounds: A Perspective Review. *Chemosphere* **2023**, *310*, 136825. [CrossRef]
8. Shahriyari, H.A.; Nikmanesh, Y.; Jalali, S.; Tahery, N. Air Pollution and Human Health Risks: Mechanisms and Clinical Manifestations of Cardiovascular and Respiratory Diseases. *Toxin Rev.* **2022**, *41*, 19–34. [CrossRef]
9. Wu, X.; Chen, Q.; He, R. Experimental research and estimation model of gasoline evaporative emissions from vehicles in China. *Sci. Total Environ.* **2024**, *918*, 170783. [CrossRef]
10. Hata, H.; Yamada, H.; Yanai, K.; Kugata, M. Modeling Evaporative Emissions from Parked Gasoline Cars Based on Vehicle Carbon Canister Experiments. *Sci. Total Environ.* **2019**, *687*, 755–764. [CrossRef]
11. Romagnuolo, L.; Yang, R.; Frosina, E.; Rizzoni, G. Physical Modeling of Evaporative Emission Control System in Gasoline-Fueled Automobiles: A Review. *Renew. Sustain. Energy Rev.* **2019**, *114*, 109308. [CrossRef]
12. Sato, K.; Kobayashi, N. Adsorption and Desorption Simulation of Carbon Canister Using n-Butane as Model Compound of Gasoline. *J. Jpn. Pet. Inst.* **2011**, *54*, 136–144. [CrossRef]
13. Huang, H.; He, Z.; Yuan, H.; Chen, Y.; Kobayashi, N. Evaluation of n-Butane Gas Adsorption Performance of Composite Adsorbents Used for Carbon Canister. *Procedia Eng.* **2011**, *24*, 42–47. [CrossRef]
14. Lee, B.-H.; Kim, Y.-J.; Lee, H.-M.; Kim, B.-J. Preparation and Characterization of Pitch-Derived Activated Carbon Pellet for Butane Adsorption. *Carbon Lett.* **2024**, *34*, 691–701. [CrossRef]
15. Lee, B.-H.; Lee, H.-M.; Chung, D.C.; Kim, B.-J. Effect of Mesopore Development on Butane Working Capacity of Biomass-Derived Activated Carbon for Automobile Canister. *Nanomaterials* **2021**, *11*, 673. [CrossRef]
16. Liu, T.; Qi, W.; Nie, L.; Wang, B. Synthesis of Sandwich-Structured Zeolite Molecular Sieves and Their Adsorption Performance for Volatile Hydrocarbons. *Materials* **2025**, *18*, 1758. [CrossRef]

17. Wu, H.; Wang, P.; Du, L.; Jin, J.; Mi, J.; Yun, J. Design of High-Humidity-Proof Hierarchical Porous P-ZIF-67(Co)–Polymer Composite Materials by Surface Modification for Highly Efficient Volatile Organic Compound Adsorption. *Ind. Eng. Chem. Res.* **2022**, *61*, 3591–3600. [CrossRef]
18. Amdebrhan, B.T. Evaluating the Performance of Activated Carbon, Polymeric, and Zeolite Adsorbents for Volatile Organic Compounds Control. Master's Thesis, University of Alberta, Edmonton, AB, Canada, 2018.
19. Lin, C.L.; Huang, C.Y.; Liu, Z.S. Enhanced Adsorption of Gaseous Naphthalene by Activated Carbon Fibers at Elevated Temperatures. *Toxics* **2024**, *12*, 537. [CrossRef]
20. Jeong, J.S.; Lee, H.M.; Kim, B.J. Preparation of Cellulose-Based Porous Carbon Fibers and Their Methylene Chloride Adsorption/Desorption Behaviors. *Energy Rep.* **2024**, *10*, 5237. [CrossRef]
21. Burchell, T.D.; Contescu, C.I.; Gallego, N.C. Activated Carbon Fibers for Gas Storage. *Act. Carbon Fiber Compos.* **2017**, *3*, 231–256.
22. Balanay, J.A.G.; Bartolucci, A.A. Adsorption Characteristics of Activated Carbon Fibers (ACFs) for Toluene: Application in Respiratory Protection. *J. Occup. Environ. Hyg.* **2014**, *11*, 489–498. [CrossRef]
23. Lin, C.L.; Cheng, Y.H.; Liu, Z.S.; Chen, J.Y. Adsorption and Oxidation of High Concentration Toluene with Activated Carbon Fibers. *J. Porous Mater.* **2013**, *20*, 775–783. [CrossRef]
24. Choi, D.; Kil, H.S.; Lee, S. Fabrication of Low-Cost Carbon Fibers Using Economical Precursors and Advanced Processing Technologies. *Carbon* **2019**, *145*, 742–756. [CrossRef]
25. Frank, E.; Hermanutz, F. Carbon Fibers: Precursors, Manufacturing, and Properties. *Macromol. Mater. Eng.* **2012**, *297*, 493–501. [CrossRef]
26. Hassan, M.F.; Sabri, M.A.; Fazal, H.; Hafeez, A. Recent Trends in Activated Carbon Fibers Production from Various Precursors and Applications—A Comparative Review. *J. Anal. Appl. Pyrolysis* **2020**, *149*, 104857. [CrossRef]
27. Frank, E.; Steudle, L.M.; Ingildeev, D. Carbon Fibers: Precursor Systems, Processing, Structure, and Properties. *Angew. Chem. Int. Ed.* **2014**, *53*, 5262–5291. [CrossRef]
28. Park, S.J.; Park, S.J. Precursors and Manufacturing of Carbon Fibers. *Carbon Fibers* **2018**, *2*, 25–47.
29. Zheng, Y.; Wang, J.; Zhu, Y.; Wang, A. Research and Application of Kapok Fiber as an Absorbing Material: A Mini Review. *J. Environ. Sci.* **2015**, *33*, 156–164. [CrossRef]
30. Wang, Y.; Zhou, M.; Zhang, X.; Ma, Y.; Wang, W. Structure and Adsorptive Properties in Wastewater Treatment of Activated Carbon Fiber Based on Kapok. In Proceedings of the 2008 2nd IEEE International Conference on Bioinformatics and Biomedical Engineering (ICBBE), IEEE, Shanghai, China, 16–18 May 2008; pp. 2131–2134.
31. Thazin, N.M.; Chaiammart, N.; Thu, M.M.; Panomsuwan, G. Effect of Pre-carbonization Temperature on the Porous Structure and Electrochemical Properties of Activated Carbon Fibers Derived from Kapok for Supercapacitor Applications. *J. Met. Mater. Miner.* **2022**, *32*, 55–64. [CrossRef]
32. Yu, W.; Huang, H.; Zhou, Y.; Xiang, R.; Zhang, X.; Chen, H. Hollow Structured Kapok Fiber-Based Hierarchical Porous Biocarbons for Ultrahigh Adsorption of Organic Dyes. *Ind. Eng. Chem. Res.* **2022**, *61*, 4114–4124. [CrossRef]
33. Biscoe, J.; Warren, B.E. An X-Ray Study of Carbon Black. *J. Appl. Phys.* **1942**, *13*, 364–371. [CrossRef]
34. Brunauer, S.; Emmett, P.H.; Teller, E. Adsorption of Gases in Multimolecular Layers. *J. Am. Chem. Soc.* **1938**, *60*, 309–319. [CrossRef]
35. Lippens, B. Studies on Pore Systems in Catalysts V. The t Method. *J. Catal.* **1965**, *4*, 319–323. [CrossRef]
36. Barrett, E.P.; Joyner, L.G.; Halenda, P.P. The Determination of Pore Volume and Area Distributions in Porous Substances. I. Computations from Nitrogen Isotherms. *J. Am. Chem. Soc.* **1951**, *73*, 373–380. [CrossRef]
37. *ASTM D5228*; Standard Test Method for Determination of Butane Working Capacity of Activated Carbon. ASTM International: West Conshohocken, PA, USA, 1992.
38. Yang, C.; Lou, Y.; Zhang, J.; Xie, X.; Xia, B. Preparation and XRD Analysis of Carbon Materials Used for Li-Ion Batteries. *Mater. Work. Mech. Second. Batter.* **2023**, *159*, 159–206.
39. Kang, D.-J.; Lee, H.-M.; An, K.-H.; Kim, B.-J. Preparation of Polyimide-Based Activated Carbon Fibers and Their Application as the Electrode Materials of Electric Double-Layer Capacitors. *Carbon Lett.* **2024**, *34*, 1653–1666. [CrossRef]
40. Popova, A.N. Crystallographic Analysis of Graphite by X-Ray Diffraction. *Coke Chem.* **2017**, *60*, 361–365. [CrossRef]
41. Kim, J.-H.; Jung, S.-C.; Lee, H.-M.; Kim, B.-J. Comparison of Pore Structures of Cellulose-Based Activated Carbon Fibers and Their Applications for Electrode Materials. *Int. J. Mol. Sci.* **2022**, *23*, 3680. [CrossRef]
42. Molina-Sabio, M.; Muñecas, M.A.; Rodríguez-Reinoso, F.; McEnaney, B. Adsorption of $CO_2$ and $SO_2$ on Activated Carbons with a Wide Range of Micropore Size Distribution. *Carbon* **1995**, *33*, 1777–1782. [CrossRef]
43. Pires, J.; Fernandes, R.; Pinto, M.; Batista, M. Microporous Volumes from Nitrogen Adsorption at 77 K: When to Use a Different Standard Isotherm? *Catalysts* **2021**, *11*, 1544. [CrossRef]
44. Sing, K.S.W. Physisorption of Nitrogen by Porous Materials. *J. Porous Mater.* **1995**, *2*, 5–8. [CrossRef]
45. Thommes, M.; Kaneko, K.; Neimark, A.V.; Olivier, J.P.; Rodriguez-Reinoso, F.; Rouquerol, J.; Sing, K.S.W. Physisorption of Gases, with Special Reference to the Evaluation of Surface Area and Pore Size Distribution. *Adsorption* **2015**, *21*, 629–650.

46. Chung, J.-T.; Hwang, K.-J.; Shim, W.-G.; Kim, C.; Park, J.-Y.; Choi, D.-Y.; Lee, J.-W. Synthesis and Characterization of Activated Hollow Carbon Fibers from Ceiba pentandra (L.) Gaertn. (Kapok). *Mater. Lett.* **2013**, *93*, 401–403. [CrossRef]
47. Lee, H.-M.; Lee, B.-H.; An, K.-H.; Park, S.-J.; Kim, B.-J. Facile Preparation of Activated Carbon with Optimal Pore Range for High Butane Working Capacity. *Carbon Lett.* **2019**, *30*, 297–305. [CrossRef]

**Disclaimer/Publisher's Note:** The statements, opinions and data contained in all publications are solely those of the individual author(s) and contributor(s) and not of MDPI and/or the editor(s). MDPI and/or the editor(s) disclaim responsibility for any injury to people or property resulting from any ideas, methods, instructions or products referred to in the content.